



Holes and cracks in rigid foam films

P. C. Petit¹, M. Le Merrer¹ and A.-L. Biance^{1,†}

¹Institut Lumière Matière, Université de Lyon, UMR 5306 Université Lyon 1-CNRS, 69622 Villeurbanne, France

(Received 27 March 2015; revised 7 May 2015; accepted 11 May 2015; first published online 11 June 2015)

The classical problem of foam film rupture dynamics has been investigated when the film interfaces exhibit very high rigidity due to the presence of specific surfactants. Two new features are reported. First, a strong deviation from the well-known Taylor–Culick law is observed. Second, crack-like patterns can be visualized in the film; these patterns are shown to appear at a well-defined film shrinkage. The key role of surface-active material on these features is quantitatively investigated, pointing to the importance of surface elasticity to describe these fast dynamical processes and thus providing an alternative tool to characterize surface elasticity in conditions extremely far from equilibrium. The origin of the cracks and their consequences on film rupturing dynamics are also discussed.

Key words: breakup/coalescence, interfacial flows (free surface), thin films

1. Introduction

Despite its apparently useless character and simplicity, the dynamics of bursting of soap bubbles has fascinated scientists for more than a century. Lucien Bull (Dubois 2000) made the first images of soap bubble bursts in 1904. The first theoretical analysis dates back to Dupré and then to Taylor (1959) and Culick (1960), where the presence of a rim at the edge of a hole created in the liquid film, collecting the liquid during its movement, was considered. The constant hole opening velocity V_c results from a balance between the rim inertia and surface tension in the film, and is given by $V_c = \sqrt{2\gamma_{eq}/(\rho h_0)}$, where γ_{eq} is the equilibrium surface tension, ρ is the liquid density and h_0 is the film thickness. These results are in good agreement with stationary experiments performed on liquid sheets (Taylor 1959) and have been extensively investigated by McEntee & Mysels (1969) in the case of soap films thicker than 50 nm. More recently, satellite formation during edge retraction (Lhuissier & Villermaux 2009b) and bubble entrapment (Bird *et al.* 2010) have been investigated as these behaviours are crucial in many applications. Destabilization of liquid sheets or bubbles indeed arises in many practical situations ranging from the

† Email address for correspondence: anne-laure.biance@univ-lyon1.fr

building material industry, e.g. when glass sheets are moulded, to foam engineering, food processing, biological membranes and environmental science (Bird *et al.* 2010). In these applications, liquids can be viscous or contain surface-active materials. In the latter situation, surface tension becomes a dynamical quantity, which depends on the local surface concentration of surfactants, and thus on the elongation of the surface; this is characterized by the surface elasticity denoted E (N m^{-1}), defined as the derivative of surface tension with respect to relative changes in surface area A ($E = (1/A)\partial\gamma/\partial A$). The effect of surface elasticity has been observed through the development of an aureole surrounding the opening hole and expanding with time (Florence & Frens 1972; Liang, Chan & Choi 1996; Lhuissier & Villermaux 2009a). However, except in the case of very viscous liquids (Debrégeas, de Gennes & Brochard-Wyart 1998), the opening dynamics always obeys the Taylor–Culick law, although some deviations have been reported by Mysels (McEntee & Mysels 1969; Florence & Mysels 1974), but hardly commented on. In this work, we investigate the dynamics of bursting of circular films generated from surfactant solutions inducing large surface elasticities and we report for the first time systematic deviations from the Taylor–Culick law. A careful analysis allows us to estimate the surface elasticity at both large compression and large compression rate in good agreement with reported data in the literature. Moreover, unexpected effects of frame size are observed through the appearance of new patterns, reminiscent of fractures or wrinkles in the film.

2. Experimental set-up

The experimental set-up consists of a circular metallic frame of radius $R = 1.5\text{--}11$ cm pulled out of a surfactant solution at different velocities to generate films with various thicknesses. The film absolute thickness is determined through a technique based on light absorption (Lastakowski *et al.* 2014; Petit *et al.* 2015), and we denote by h_0 the initial average thickness of the film. Film rupture is initiated by approaching a heated needle and is recorded via a high-speed camera (10000 Hz, Photron SA-4). An image sequence is reported in figure 1(a), where we measure the radius r of the expanding hole versus time, as shown in figure 1(b). Surfactant solutions are produced in a 10–90 % glycerol–water mixture in which a dye (Brilliant Black BN 60 %, Sigma, 5 g l^{-1}) is added. They contain 3.3 g l^{-1} of sodium lauryl ether sulphate (SLES, Stepan), 1.7 g l^{-1} of cocamidopropyl betaine (CAPB, Goldschmidt) and myristic acid (MAc, Fluka) in the concentrations C described in table 1. The surface elasticities of similar solutions are well characterized in the literature (Mitrinova *et al.* 2013a) and span over two orders of magnitude when the concentration C of MAc is varied as reported in table 1. These elastic moduli are attributed to the surface properties of the adsorbed layer of MAc, whose surface concentration is expected to increase with C up to saturation of the surface (Golemanov *et al.* 2008). At the same time, micelles of the two cosurfactants (SLES and CAPB) help to solubilize the poorly soluble fatty acid.

3. Results

Some remarkable features can be underlined. At first, the opening velocity is constant as predicted by the Taylor–Culick law but smaller than expected (figure 1b). Moreover, an aureole that has already been described in the past (Florence & Frens 1972; Liang *et al.* 1996; Lhuissier & Villermaux 2009a) is observed through spatial

Holes and cracks in rigid foam films

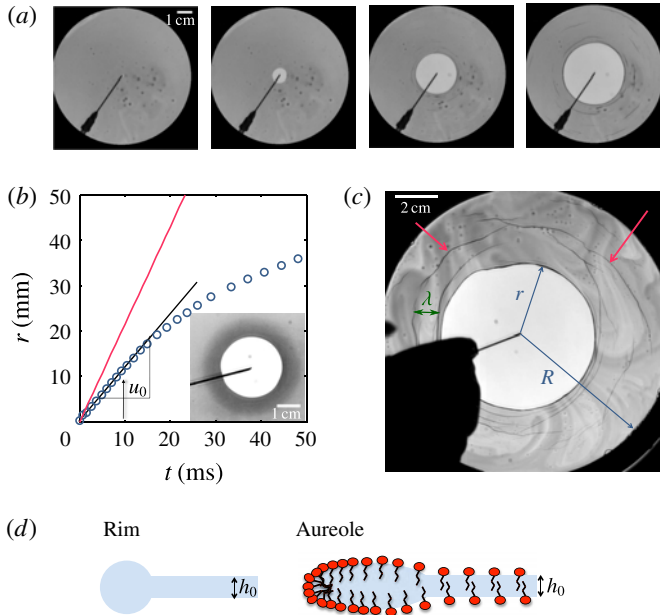


FIGURE 1. (a) Image sequence of a foam film rupture ($h_0 = 10 \mu\text{m}$, solution E – table 1). The time lapse between images is 8 ms. (b) Radius r of the hole versus time t ($h_0 = 10 \mu\text{m}$, solution E). The red line represents the prediction of Taylor–Culick, while the black line shows the initial opening at constant velocity u_0 . The arrow denotes first crack apparitions. Inset: picture of a ruptured foam film (solution C) which highlights aureole formation. (c) Picture of a foam film (solution E) 37 ms after its breaking. The arrows highlight crack-like patterns, which appear during the hole opening. Here, R corresponds to the size of the frame, while λ is the characteristic length between two cracks (see text). (d) Scheme of the film shape in the case of Taylor–Culick (free interfaces and rim) and in the case of inhomogeneous surfactant repartition (aureole).

Solution	A	B	C	D	E	F
C (mM)	—	0.055	0.11	0.22	0.88	2.2
γ_{eq} (mN m ⁻¹)	29	29	27	26	23	22
E_{od} (mN m ⁻¹)	4	50	90	200	400	400
$E_0(u_0)$ (mN m ⁻¹)	60	200	2000	5000	2×10^4	4×10^4
$E_0(\text{cracks})$ (mN m ⁻¹)	—	—	90	200	300	300

TABLE 1. Properties of the surfactant solutions used in the experiments: MAC concentration C , equilibrium surface tension γ_{eq} and surface elasticities. The surface tension γ_{eq} and elastic modulus E_{od} reported have been measured by Mitrinova *et al.* (2013a) for similar solutions (without glycerol and dye). The surface tension is determined by the static shape of the pendant drop whereas the surface elastic modulus is measured by the oscillating drop method for small deformation (0.2–4%) at a frequency of 0.2 Hz. Here, $E_0(u_0)$ corresponds to the elasticity deduced from the initial hole velocity using (4.1) and $E_0(\text{cracks})$ corresponds to the elasticity deduced from the hole radius at which cracking occurs using (4.2).

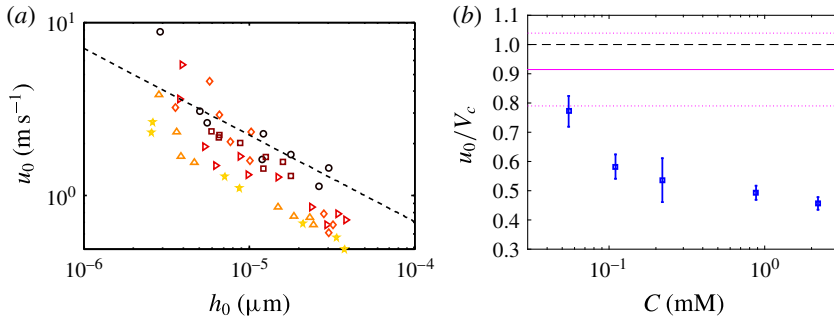


FIGURE 2. (a) Initial opening velocity u_0 of the hole as a function of the film thickness h_0 for $R=3$ cm. The MAc concentration C increases from dark to light points: solutions A (\circ), B (\square), C (\triangleright), D (\diamond), E (\triangle) and F (\star). (b) Initial opening velocity normalized by the Culick velocity u_0/V_c as a function of C (error bars: 95% confidence intervals). The magenta solid line shows the value measured for $C = 0$, with error bars shown by the dotted lines. The values of u_0/V_c are extracted by performing a least-squares percentage fit for each solution, with weights taking into account the $1 \mu\text{m}$ error in thickness measurements. In both panels, the black dashed lines represent the Taylor–Culick law.

variations of the transmitted light, especially for the less rigid interfaces (inset of figure 1b). The aureole front propagates at a velocity denoted u_f . Then, some dark patterns are observed (see arrows in figure 1c), which we denote cracks in the following. This apparition coincides with a decrease of the opening velocity (figure 1b), as the presence of these cracks modifies the bursting dynamics.

The initial opening velocity u_0 is represented in figure 2(a) as a function of the initial film thickness h_0 for various solutions. Without MAc (solution A of table 1), the velocity follows the Taylor–Culick law (\circ), which is consistent with interfaces of low elasticity. However, in the presence of MAc, the initial velocity is lower than in the previous case. For each MAc concentration, the initial velocity is proportional to $1/\sqrt{h_0} \propto V_c$. For each solution and different thicknesses, we thus extract the initial opening velocity normalized by the Culick velocity. This quantity decreases when the MAc concentration increases (figure 2b), that is, for larger surface elastic moduli (Mitrinova *et al.* 2013a).

During the film opening, orthoradial cracks (perpendicular to the direction of opening) appear in the film (figure 1a,c), at a well-defined radius of the hole r_p . Some specific irregular fold-like patterns and filaments have previously been reported by McEntee & Mysels (1969), although not directly comparable to our observations. For a given solution, figure 3(a) shows that the ratio r_p/R is independent of the frame radius (for $R = 1.5\text{--}11$ cm) and almost independent of the film thickness (for $h_0 = 2\text{--}20 \mu\text{m}$). The cracks thus appear for a well-defined critical compression of the interface. Figure 3(b) shows that this critical compression decreases with MAc concentration and the surface modulus. This critical compression is so large for solution B that we cannot define it accurately.

4. Discussion

These two observations concerning the initial opening velocity and the onset compression for cracks can be rationalized following the framework initially proposed

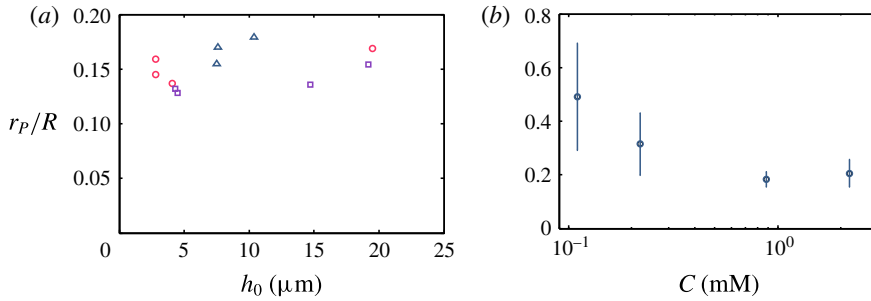


FIGURE 3. (a) Critical compression of the interface for crack formation r_p/R as a function of the initial thickness h_0 for solution E and different frame radii $R = 1.5$ cm (\circ), $R = 3$ cm (\square) and $R = 11$ cm (\triangle). (b) The critical compression r_p/R averaged for thicknesses $h_0 = 2-35$ μm and $R = 3$ cm, as a function of MAC concentration C .

by Frankel & Mysels (1969) for the theoretical description of aureoles. They considered that surfactants are insoluble, which is reasonable at the time scale considered here: the duration of the opening R/u_0 , typically 30 ms, is smaller than the surfactant desorption time τ . Indeed, although these processes are likely to be dominated by surfactant exchange with micelles in our systems (Golemanov *et al.* 2008), a lower bound for τ is provided by the diffusion time across the film thickness $h_0^2/D \approx 40$ ms–2 s (for $h_0 = 2-40$ μm and $D = 10^{-10}$ m^2 s^{-1}). Adsorption times longer than 30 ms for myristic acid in these systems have also been reported (Mitrinova *et al.* 2013b). A compressive shock thus propagates at the surface of the film. The liquid is collected in an extended rim – an aureole – visible in figure 1(b) (inset) and whose shape depends on the surface tension, film thickness and surface elasticity.

Viscous effects have also been neglected. Indeed, as no shear takes place within the film thickness, the characteristic Reynolds number and surface Reynolds numbers read $Re = u_0 R/\nu \gg 1$ and $Re_s = \rho u_0 R h_0/\kappa$ respectively, with ν the kinematic bulk viscosity and κ the intrinsic surface viscosity. Surface viscous dissipation cannot be neglected *a priori* if values of κ measured at 0.2 Hz are considered (Golemanov *et al.* 2008; Costa 2012). However, the surface viscosity is expected to collapse at large frequencies, as shown in experiments and modelling (Lucassen & Van Den Tempel 1972). Eventually, the observation of a constant initial velocity proportional to $1/\sqrt{h_0} \propto V_c$ (figures 1b and 2) is a key indication that inertia (and not viscous effects) is dominant in this problem.

4.1. Deviation from the Taylor–Culick law

As mentioned above, we can neglect surface viscous effects. The deviation from the Taylor–Culick law, observed in the presence of a certain type of surfactants, is then attributed to surface elasticity. To take this effect into account, the dynamics of the rim is now controlled by the balance between inertia and surface tension spatial gradient. We assume here that the surface elasticity is constant up to a certain compression. In this particular case, the velocity of the aureole front (delimiting the frontier with the zone of undisturbed film whose thickness is still $h = h_0$) simply reads $u_f = \sqrt{2E_0/(\rho h_0)} = V_c \sqrt{E_0/\gamma_{eq}}$, which can be seen as a two-dimensional analogue of sound (compression) velocity. The opening hole velocity can also be determined by solving the self-similar profile of the aureole and applying mass conservation

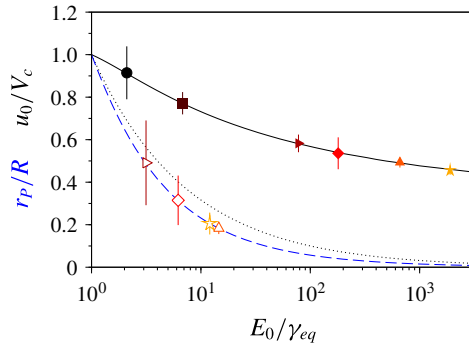


FIGURE 4. Solid black line: numerical prediction for the normalized hole velocity $u_0/V_c = f(E_0/\gamma_{eq})$ for radial bursting ((4.1) and appendix A). The dashed line corresponds to $u_0/V_c = \sqrt{\gamma_{eq}/E_0}$ expected for unidimensional bursting (Frankel & Mysels 1969). Blue dashed line: prediction for the critical radius at which cracks appear, $r_p/R = \sqrt{\gamma_{eq}/E_0} f(E_0/\gamma_{eq})$ (4.2). The solid (respectively empty) symbols correspond to the experimental data from figure 2 (respectively figure 3), from which we determine the elastic moduli $E_0(u_0)$ (respectively $E_0(\text{cracks})$). The same symbols and colours are used as in figure 2(a).

(see appendix A). No analytical solution is provided in the considered radial geometry, but numerical resolution shows that

$$u_0 = V_c f(E_0/\gamma_{eq}), \quad (4.1)$$

where f is the decreasing function determined numerically (see appendix A) and reported in figure 4. It is thus still proportional to the Taylor–Culick velocity V_c and decreases with the interfacial elasticity E_0 , which is consistent with the experimental observations of figure 2.

From our experimental measurements of u_0 (figure 2) and using the numerical solution of (4.1) represented in figure 4, an interfacial elasticity $E_0(u_0)$ can be deduced (figure 4) for each solution, which is reported in table 1 as a function of the MAc concentration. These data are compared with measurements of the surface moduli E_{od} from the oscillating drop method performed by Mitrinova *et al.* (2013a). They show the same qualitative variation with C despite a discrepancy in the absolute values obtained. However, the shrinkage amplitude and the compression time scales differ by several orders of magnitude, and the surfactant monolayer at the interface is expected to be highly non-Newtonian (Lucassen & Van Den Tempel 1972; Costa 2012).

4.2. Crack appearance

Snapshot inspection also shows that cracks appear when the compressive surface wave (i.e. the aureole front) reaches the metallic frame of the film. Cracks are thus expected for

$$\frac{r_p}{R} = \frac{u_0}{u_f} = \sqrt{\frac{\gamma_{eq}}{E_0}} f\left(\frac{E_0}{\gamma_{eq}}\right). \quad (4.2)$$

This prediction, represented in figure 4, is indeed in good agreement with our observations: the hole radius when cracks appear r_p increases with the frame radius R

and decreases with the surface elasticity probed through MAc concentration variations, as shown in figure 3. Eventually, this critical compression does not depend on the film thickness h_0 , showing that elasticity is not affected by confinement in the experimental configuration tested.

From this measured critical compression, another value of the surface elasticity, denoted $E_0(\text{cracks})$, can therefore be determined using (4.2); this is also plotted in figure 4. These experimental values are reported for the different MAc concentrations in table 1. In this case, very good agreement is obtained with the measured value of the surface modulus (Mitrinova *et al.* 2013a), which confirms that the cracks arise from a compression of the aureole when its front reaches the frame.

It should be noted that the values of surface elasticity deduced from our two methods may differ. This is, however, expected due to our strong hypothesis of constant elasticity. Indeed, while the aureole front velocity only depends on the surface elasticity at very low compression rate (at the edge of the undisturbed film), the hole opening velocity modelling takes into account the elasticity through large interface compression. For large deformation, it is expected that the constant elasticity model will fail: at large compression, the myristic acid surface concentration increases, which should result in larger elasticity, as can be inferred from the moduli dependence upon C (Mitrinova *et al.* 2013a). The effective modulus $E_0(u_0)$ should then deviate more from measurements at small deformations performed by the oscillating bubble technique (Mitrinova *et al.* 2013a).

In addition, the effect of elasticity has indirect consequences on some features of foam film rupture. For example, no flapping or transverse destabilization of the rim was observed for our rigid soap films, in contrast to observations on low-elasticity films and theoretical predictions (Lhuissier & Villermaux 2009b); however, the reduced rim velocity could prevent the flapping instability from developing, and subsequent film atomization (Lhuissier & Villermaux 2009b).

4.3. Crack-like patterns

Let us now discuss the observed crack-like patterns. During the fast deformation of the surface, the surfactants behave as an insoluble monolayer, comparable to a lipid monolayer experiencing a compression in a Langmuir trough (Lee 2008). In this case, above a critical compression, such a monolayer can behave differently depending on its structure. If it is liquid-like, it ejects the molecules in the bulk in the form of vesicles or bilayers. If it is solid-like, it can bend as an elastic sheet or fracture as a fragile material.

Although our experiment does not provide a microscopic characterization of this transient surface structure, the crack pattern can be macroscopically characterized. In particular, even though the cracks are irregularly distributed, the number of cracks per radial segment can be counted; the deduced characteristic length between two cracks denoted λ (figure 1c) is reported in figure 5 as a function of MAc concentration C (a) and film thickness h_0 (b).

The increase of λ with C can be expected in the abovementioned situations. On the one hand, for higher bulk concentration, solubilization of interfacial surfactants is more difficult, hence a reduced number of vesicles or bilayers are expelled. On the other hand, a more concentrated solid-like layer will also exhibit a higher bending modulus and the wavelength of the elastic ripples is expected to increase with this modulus (Cerdea & Mahadevan 2003). The decrease of the characteristic length with the film thickness h_0 is more unexpected. For the solid-like behaviour, a thinner

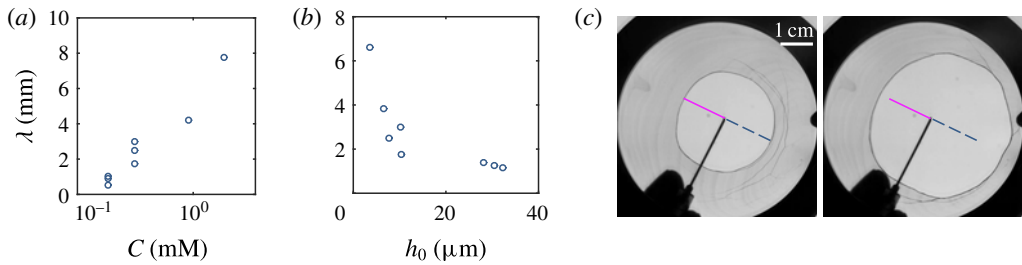


FIGURE 5. (a) Characteristic length λ between two cracks as a function of MAC concentration C for $h_0 = 11 \pm 3 \mu\text{m}$. (b) Characteristic length λ as a function of the film thickness h_0 for solution D. (c) Bursting of a soap film of thickness $h_0 = 3 \mu\text{m}$ (solution E). The time lapse between the two images is 9 ms, and the two lines highlight the velocity inhomogeneities.

elastic sheet will bend more easily than a thicker one, thus exhibiting smaller ripple wavelength when buckled (Landau & Lifshitz 1975), in contrast to our observations. If the cracks correspond to monolayer collapse by vesicle formation, it should not be affected by the film thickness. However, varying film thickness also has an effect on the velocity of compression or shrinkage rate. This parameter induces dynamical structural change in the surfactant monolayers (as it does in bulk crystallization processes for example (Cabane & Hénon 2003)). Finally, a complete understanding of the origin of these crack-like patterns would require some local high-speed imaging structural analysis, which is beyond the scope of the present paper.

The presence of these irregular cracks has direct consequences on the hole opening dynamics. Indeed, when the aureole reaches the metallic frame, the hole opening slows down (and even stops for the thinner rigid films) and then irregularly accelerates in the region where the cracks appear. This feature is reported in figure 5(c). Moreover, a velocity discontinuity in the liquid is observed, the outer region being at rest whereas the inner region is deformed.

5. Conclusion

To conclude, we have shown that modification of the chemistry of surfactant solutions can have a strong influence on macroscopic dynamical processes, as observed in various situations in foams and foam films (Mysels, Frankel & Shinoda 1959; Couder, Chomaz & Rabaud 1989; Durand & Stone 2006; Cohen-Addad, Hohler & Pitois 2013; Seiwert *et al.* 2013; Petit *et al.* 2015). However, here we have investigated this effect under large deformations and in a fast dynamical process, i.e. at large Reynolds numbers, where the effects of molecular scales and surfactants are expected to be negligible.

The initial constant velocity opening dynamics is well described taking into account the surface elasticity of the interfaces and was shown to be reduced at high surface modulus. This may be responsible for the inhibition of rim fragmentation and droplet ejection usually reported in liquid film ruptures (Lhuissier & Villermaux 2009b). Further studies should determine the role of the ejected droplets in rupture propagation in macroscopic foams; the stability of these systems is indeed known to depend dramatically on the surface elastic properties (Rio & Bianco 2014). However, finite-size effects soon become crucial: when the elastic compression surface wave reaches the border of the frame, crack-like patterns, where velocity discontinuities

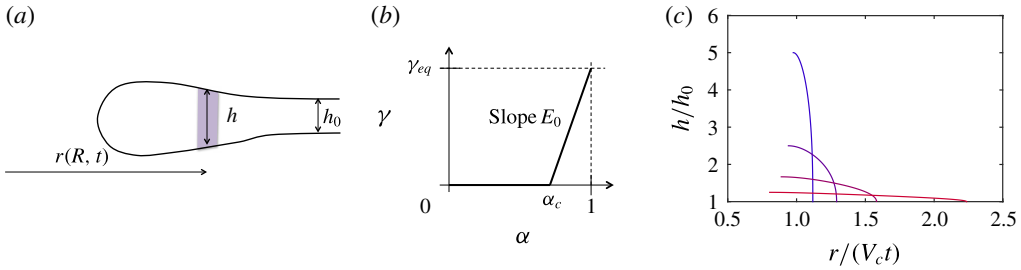


FIGURE 6. (a) Profile of the film and notations; (b) variations of surface tension γ versus shrinkage α in the simplified constant elasticity modelling; (c) h/h_0 as a function of $r/(V_c t) = \sqrt{2w/V_c^2}$ for radial bursting and different values of α_c (0.2, 0.4, 0.6, 0.8 from top to bottom at the origin).

are observed, appear in the foam film. Determination of the origin of cracks, their microscopic structure, their location and number, and how they control film opening dynamics remains a challenge to tackle.

Acknowledgement

The authors thank G. Simon for his help in setting up the experiment.

Appendix A

A.1. Equations for radial bursting

We describe the radial bursting dynamics of a foam film of initially uniform thickness h_0 and include the effect of dynamic surface tension as first proposed by Frankel & Mysels (1969): the surface tension γ is assumed to depend only on the shrinkage of the surface α which by mass conservation is related to the film thickness $\alpha = h_0/h$. We denote the surface elasticity by $E(\alpha) = d\gamma/d\alpha$. As viscous terms are negligible, the capillary forces are balanced by the fluid inertia. Variations of fluid velocity across the film are also neglected and equations are averaged over h . These equations can be explicitly solved in the unidimensional case (Frankel & Mysels 1969). However, in the case of radial bursting, a numerical resolution is necessary.

We consider a material element that initially has the position R (i.e. that has Lagrangian variables (R, t)). At instant t , its position is $r(R, t)$ and its thickness is $h(R, t)$ (figure 6a). The fluid velocity is $u = \partial r/\partial t$ and the shrinkage is defined as $\alpha = h/h_0 \partial r^2/\partial R^2 = (r/R) \partial r/\partial R$. The momentum balance on the fluid element yields

$$\rho r h \frac{\partial u}{\partial t} = 2r \frac{\partial \gamma}{\partial r}, \tag{A 1}$$

which can be rewritten as

$$\frac{\partial u}{\partial t} = \frac{2E(\alpha)}{\rho h_0} \frac{r}{R} \frac{\partial \alpha}{\partial R} = U_\alpha^2 \frac{r}{R} \frac{\partial \alpha}{\partial R}, \tag{A 2}$$

in which we have defined the characteristic velocity

$$U_\alpha = \sqrt{\frac{2E(\alpha)}{\rho h_0}}. \tag{A 3}$$

Following the analysis of Frankel & Mysels (1969), we are looking for self-similar solutions in the form $r/t = f(R/t)$. We define the variables $W = R^2/(2t^2)$ and $w = r^2/(2t^2)$ (w and W have the dimensions of square velocities) and we expect $w = w(W)$. The relative shrinkage is also set by $\alpha = dw/dW$. Starting from (A 2), we find

$$\frac{W}{w} \left[1 - \frac{W}{w} \frac{dw}{dW} \right] \frac{dw}{dW} = \left[U_{\alpha=dw/dW}^2 - \frac{2W^2}{w} \right] \frac{d^2w}{dW^2}. \tag{A 4}$$

A first piece of information on the film dynamics can be inferred from this equation: far from the hole, i.e. for large W , the film should remain undisturbed, which corresponds to $w = W$ and $dw/dW = 1$. This condition combined with (A 4) yields $[U_{\alpha=1}^2 - ((2W^2)/w)](d^2w/dW^2) = 0$, which implies that the matching with the disturbed film can only be carried out at $W = W_0 = U_{\alpha=1}^2/2$. The velocity of the front of the aureole, or extended rim corresponding to the disturbed film, is thus given by $u_f = U_{\alpha=1}$ (Frankel & Mysels 1969).

Finally, the complete aureole profile and hole receding velocity will depend on the form of the elasticity versus shrinkage.

A.2. Numerical resolution for a constant elasticity model

We consider at first order a model of constant elasticity E_0 , as described in figure 6(b). We introduce here α_c , which corresponds to the maximum shrinkage the film can endure. For $\alpha > \alpha_c$, the surface elasticity is constant and reads

$$\frac{d\gamma}{d\alpha} = E_0 = \gamma_{eq} \frac{1}{1 - \alpha_c} \tag{A 5}$$

and then

$$U_\alpha = U_0 = \sqrt{\frac{2E_0}{\rho h_0}} = \sqrt{\frac{E_0}{\gamma_{eq}}} V_c, \tag{A 6}$$

where $V_c = \sqrt{2\gamma_{eq}/(\rho h_0)}$ is the Culick velocity.

Let us note that the aureole (the shock) is observed only if the compressive wave propagation velocity U_α is larger than V_c , i.e. $E_0 \geq \gamma_{eq}$. When $\alpha > \alpha_c$, (A 4) can be written as

$$\frac{W}{w} \left[1 - \frac{W}{w} \frac{dw}{dW} \right] \frac{dw}{dW} = \left[U_0^2 - \frac{2W^2}{w} \right] \frac{d^2w}{dW^2}. \tag{A 7}$$

In non-dimensionalized form (stating $\tilde{W} = 2W/V_c^2$ and $\tilde{w} = 2w/V_c^2$), this equation reduces to

$$\frac{\tilde{W}}{\tilde{w}} \left[1 - \frac{\tilde{W}}{\tilde{w}} \frac{d\tilde{w}}{d\tilde{W}} \right] \frac{d\tilde{w}}{d\tilde{W}} = \left[\frac{1}{1 - \alpha_c} - \frac{2\tilde{W}^2}{\tilde{w}} \right] \frac{d^2\tilde{w}}{d\tilde{W}^2}, \tag{A 8}$$

with the following two boundary conditions. For $\tilde{W} = 0$, at the hole, we have the maximum shrinkage (minimum value of α_c): $(d\tilde{w}/d\tilde{W})(\tilde{W} = 0) = \alpha_c$. For $\tilde{W} = \tilde{W}_0 = 1/(2(1 - \alpha_c))$, at the aureole front, the solution should match the undisturbed film solution $\tilde{w}(\tilde{W}_0) = \tilde{W}_0$.

This equation is solved numerically with a shooting method. From the function $w(W)$, we can deduce the thickness profile, using the relation $h/h_0 = 1/(dw/dW)$ for

different elasticities (figure 6c). As the elasticity increases (i.e. as α_c becomes closer to 1), we find that the aureole is thinner and wider, while for $E_0 = \gamma_{eq}$ (corresponding to $\alpha_c = 0$), one recovers a punctual rim receding at the Taylor–Culick velocity V_c .

We can also estimate the initial hole velocity $u_0 = \sqrt{2w(W=0)}$, which is shown in figure 4 as a function of the ratio E_0/γ_{eq} . We also observe that the results obtained deviate from those obtained for unidimensional bursting (Frankel & Mysels 1969), especially for large elasticities, emphasizing the crucial role of radial geometry.

References

- BIRD, J. C., DE RUITER, R., COURBIN, L. & STONE, H. A. 2010 Daughter bubble cascades produced by folding of ruptured thin films. *Nature* **465** (7299), 759–762.
- CABANE, B. & HÉNON, S. 2003 *Liquides – Solutions, Dispersions, Gels*. Belin.
- CERDA, E. & MAHADEVAN, L. 2003 Geometry and physics of wrinkling. *Phys. Rev. Lett.* **90** (7), 074302.
- COHEN-ADDAD, S., HOHLER, R. & PITOIS, O. 2013 Flow in foams and flowing foams. *Annu. Rev. Fluid Mech.* **45**, 241–267.
- COSTA, S. 2012 Rhéologie multi-échelle des mousses liquides. PhD thesis, Université Paris-Est Marne La Vallée.
- COUDER, Y., CHOMAZ, J. M. & RABAUD, M. 1989 On the hydrodynamics of soap films. *Physica D* **37** (1–3), 384–405.
- CULICK, F. E. C. 1960 Comments on a ruptured soap film. *J. Appl. Phys.* **31** (6), 1128–1129.
- DEBRÉGEAS, G., DE GENNES, P.-G. & BROCHARD-WYART, F. 1998 The life and death of ‘bare’ viscous bubbles. *Science* **279**, 1704–1707.
- DUBOIS, P. 2000 Exposer marey. L’image, le mouvement et la pensée. *Études Photogr.* **8**, 146–152.
- DURAND, M. & STONE, H. A. 2006 Relaxation time of the topological T1 process in a two-dimensional foam. *Phys. Rev. Lett.* **97**, 226101.
- FLORENCE, A. T. & FRENS, G. 1972 Aureole profile in bursting soap films – surface-tension and surface relaxation in rapidly compressed monolayers. *J. Phys. Chem.* **76** (21), 3024–3029.
- FLORENCE, A. T. & MYSELS, K. J. 1974 Bursting of soap films. VI. Effect of surfactant purity. *J. Phys. Chem.* **78** (3), 234–235.
- FRANKEL, S. & MYSELS, K. J. 1969 Bursting of soap films. 2. Theoretical considerations. *J. Phys. Chem.* **73** (9), 3028–3038.
- GOLEMANOV, K., DENKOV, N. D., TCHOLAKOVA, S., VETHAMUTHU, M. & LIPS, A. 2008 Surfactant mixtures for control of bubble surface mobility in foam studies. *Langmuir* **24** (18), 9956–9961.
- LANDAU, L. D. & LIFSHITZ, E. M. 1975 *Elasticity Theory*. Pergamon.
- LASTAKOWSKI, H., BOYER, F., BIANCE, A. L., PIRAT, C. & YBERT, C. 2014 Bridging local to global dynamics of drop impact onto solid substrates. *J. Fluid Mech.* **747**, 103–118.
- LEE, K. Y. C. 2008 Collapse mechanisms of Langmuir monolayers. *Annu. Rev. Phys. Chem.* **59**, 771–791.
- LHUISSIER, H. & VILLERMAUX, E. 2009a Destabilization of flapping sheets: the surprising analogue of soap films. *C. R. Méc.* **337** (6–7), 469–480.
- LHUISSIER, H. & VILLERMAUX, E. 2009b Soap films burst like flapping flags. *Phys. Rev. Lett.* **103** (5), 054501.
- LIANG, N. Y., CHAN, C. K. & CHOI, H. J. 1996 Dynamics of the formation of an aureole in the bursting of soap films. *Phys. Rev. E* **54** (4), R3117–R3120.
- LUCASSEN, J. & VAN DEN TEMPEL, M. 1972 Dynamic measurements of dilational properties of a liquid interface. *Chem. Engng Sci.* **27** (6), 1283–1291.
- MCENTEE, W. R. & MYSELS, K. J. 1969 Bursting of soap films. I. An experimental study. *J. Phys. Chem.* **73** (9), 3018–3028.
- MITRINOVA, Z., TCHOLAKOVA, S., GOLEMANOV, K., DENKOV, N., VETHAMUTHU, M. & ANANTHAPADMANABHAN, K. P. 2013a Surface and foam properties of SLES plus CAPB plus fatty acid mixtures: effect of pH for C12–C16 acids. *Colloids Surf. A* **438**, 186–198.

- MITRINOVA, Z., TCHOLAKOVA, S., POPOVA, Z., DENKOV, N., DASGUPTA, B. R. & ANANTHAPADMANABHAN, K. P. 2013*b* Efficient control of the rheological and surface properties of surfactant solutions containing C8–C18 fatty acids as cosurfactants. *Langmuir* **29** (26), 8255–8265.
- MYSELS, K. J., FRANKEL, S. & SHINODA, K. 1959 *Soap Films: Studies of their Thinning* Pergamon Press.
- PETIT, P., SEIWERT, J., CANTAT, I. & BIANCE, A.-L. 2015 On the generation of a foam film during a topological rearrangement. *J. Fluid Mech.* **763**, 286–301.
- RIO, E. & BIANCE, A.-L. 2014 Thermodynamic and mechanical timescales involved in foam film rupture and liquid foam coalescence. *Chem. Phys. Chem.* **15** (17), 3692–3707.
- SEIWERT, J., MONLOUBOU, M., DOLLET, B. & CANTAT, I. 2013 Extension of a suspended soap film: a homogeneous dilatation followed by new film extraction. *Phys. Rev. Lett.* **111** (9), 094501.
- TAYLOR, G. 1959 The dynamics of thin sheets of fluid. 3. Disintegration of fluid sheets. *Proc. R. Soc. Lond. A* **253** (1274), 313–321.